

# A novel approach to estimating urban land surface temperature by the combination of geographically weighted regression and deep neural network models

Jia Sqi<sup>a</sup>, Wang Yuhong<sup>a,\*</sup>, Chen Ling<sup>b</sup>, Bi Xiaowen<sup>a</sup>

<sup>a</sup> The Hong Kong Polytechnic University, Hung Hom, Kowloon, Hong Kong

<sup>b</sup> Xidian University, Xi'an 710071, China

## ARTICLE INFO

### Keywords:

Urban heat island  
Land surface temperature  
Neural network  
Geographically weighted regression

## ABSTRACT

Growing concerns on excessive urban heat call for better approaches to modeling urban thermal environment and developing effective mitigation strategies. A hybrid model integrating the geographically weighted regression (GWR) and deep neural network (DNN) was developed to estimate land surface temperature (LST). This model was compared with three other data-driven approaches to predicting LST, including the ordinary least squares (OLS) regression, GWR, and DNN. Sixteen satellite image datasets (a total of 155,728 data points) during a four-year period in Hong Kong were used for model development, validation, and comparison. The datasets cover two distinguishable geographical regions and consist of sixteen explanatory variables from five groups, including (1) land use and land cover (LULC) composition and surface characteristics, (2) LULC configuration, (3) urban form, (4) anthropogenic activities, and (5) location and local climate. The results indicate that the hybrid model performs the best in terms of model fitness and prediction accuracy, with  $R^2$  equal to 0.85 and 0.73 and the mean squared error (MSE) equal to 0.52 and 0.70 in the two regions, respectively. Compared to the OLS, DNN, and GWR models, the overall  $R^2$  for all the datasets of the hybrid model increases by 97.3%, 16.6%, and 6.9%, respectively. The promising result of the hybrid model is due to its ability to capture both spatial heterogeneity and address possible correlations between explanatory variables. Sensitivity of LST to various explanatory variables is also discussed and strategies to mitigate excessive heat are recommended. This study is anticipated to contribute to model development in urban LST estimation and quantitative evaluation of those factors driving LST variations.

## 1. Introduction

Urban heat island (UHI) is a well-known and extensively studied phenomenon. Warmer temperatures in urban areas as compared to those at pre-development levels and in neighboring rural areas create many adverse effects to human societies (Konopacki and Akbari, 2002; Schwarz et al., 2012). With more people moving to cities, urban thermal environment has become more of a concern or even a challenge to urban dwellers, especially to those without access to air conditioning. Moreover, the general trend of global warming and extreme heat events associated with climate change pose additional threats to people living in cities (Ren et al., 2022; Fagan, 2008). A

\* Corresponding author at: Block Z, The Hong Kong Polytechnic University, 11 Yuk Choi Rd, Hung Hom, Hong Kong.

E-mail addresses: [18104641R@connect.polyu.hk](mailto:18104641R@connect.polyu.hk) (J. Sqi), [yuhong.wang@polyu.edu.hk](mailto:yuhong.wang@polyu.edu.hk) (W. Yuhong), [chenling@xidian.edu.cn](mailto:chenling@xidian.edu.cn) (C. Ling), [xiaowen.bi@polyu.edu.hk](mailto:xiaowen.bi@polyu.edu.hk) (B. Xiaowen).

recent study found that both urban thermal environment and human thermal comfort keep deteriorating in a large number of cities in China (Ren et al., 2022). In particular, greenspace loss in urbanization causes thermal environment degradation and deprivation of residents' access to natural cooling (Dong et al., 2022).

UHI may be directly identified through recorded weather data at different locations in a city. Besides knowing the heat islands, it is also important for city planners and managers to understand those factors that drive urban climate variations and take proper actions to mitigate the UHI effect. Land use and land cover (LULC) composition and configuration are found to be the main driving factors of the UHI effect (Xie et al., 2013), followed by heat generated by anthropogenic activities (Howard, 1818; Oke, 1982). If connections between urban temperatures and LULC and the socioeconomic factors can be quantified, planning actions may be optimized to balance and improve the urban thermal environment.

Numerous models have been developed to estimate urban temperatures with the aim to reveal those factors that contribute to UHI effect. The dependent variables are either air temperature or land surface temperature (Guo et al., 2015), and the influencing factors include a wide range of variables, depending on the nature of the models and the availability of relevant data. The models may be generally divided into two categories (Guo et al., 2015; Li et al., 2011). The first category relies on simulation models based on in-situ measurements or laboratory data. Examples include energy balance models such as the urban canopy model (UCM) and building energy model (BEM) (Masson, 2000; Oke et al., 1999), and dynamic numerical simulation methods such as computational fluid dynamics (CFD) (Wang and Li, 2016; Yuan et al., 2022). Some studies also attempted to couple a UCM or BEM with a large-scale atmospheric and climate model such as the Weather Research and Forecasting (WRF) model for urban climate simulation (Kusaka et al., 2012; Wong et al., 2019). Simulation-based approaches have the advantage of capturing the fundamental physical processes behind thermal environment variations. However, not all the contributing factors may be easily identified and included in the simulation models. In addition, the effects of LULC composition and socioeconomic factors may not be readily revealed, unless sensitivity analysis is performed (Oke et al., 1999; Jia and Wang, 2020). If the CFD models are used, the analysis domain size is typically limited due to the complexity of creating a large-size model and the long computational time (Deng and Wu, 2013; Gobakis et al., 2011; Ketterer and Matzarakis, 2015).

The second category includes data-driven approaches. With the development of remote sensing technology, remote sensing-based data such as the land surface temperature (LST) are increasingly used to examine UHI effect for its wide temporal and spatial coverage. Linear regression models are commonly used to explore the relationships between temperature and various factors, including LULC composition (Chen et al., 2006), urban forms (Alcoforado and Andrade, 2005), landscape pattern (Li et al., 2011), population density (Xiao et al., 2008), satellite-based indices, e.g., normalization differential vegetation index (NDVI), normalization differential build-up index (NDBI), normalization differential bareness index (NDBaI) (Guo et al., 2015; Yuan and Bauer, 2007), and topographic features (Li et al., 2010). In a conventional regression model (e.g., ordinary least squares or OLS), the coefficients of the independent variables are fixed at different locations. Spatial regression models have been developed to accommodate geographically non-stationary relations between temperature and influencing factors (Li et al., 2010; Zhao et al., 2018). For example, Yin et al. used the spatial lag model (SLM) and the spatial error model (SEM) to predict LST based on LULC composition and urban form indicators (Yin et al., 2018a). Zhao et al. investigated how underlying biophysical attributes affect LST variations based on the geographically weighted regression (GWR) (Zhao et al., 2018). Spatial regression models generally provide better fitness as compared to the non-spatial models; however, the complex interactions between the influencing factors are difficult to be modelled (Du et al., 2020).

Under the data-driven approach, artificial neural network (ANN) has also been used to predict temperature. ANN has the capability of capturing non-linear relationships and the complicated interactions between data (Gardner and Dorling, 1998; Shaker and Ehlinger, 2014). As early as in 1988, an ANN model was developed to predict hourly air temperature and satisfactory results were reported (Mihalakakou et al., 1998). By comparing the results from an ANN model and a multiple linear regression model, Kim and Baik (2002) concluded that the ANN model improves prediction accuracy by up to 6.5% (Kim and Baik, 2002). With the recent development of computational power, deep neural networks (DNN) have gained increasing popularity. DNN employs deep architectures in neural networks and hence can represent functions with higher complexity (Liu et al., 2017). For instance, Oh et al. (2020) used DNN to analyze and predict temporal and spatial UHI behaviors from 54 observatories in Seoul and reported satisfactory results (Oh et al., 2020). Most previous studies using ANN or DNN approaches are based on meteorological data collected from a limited number of measurement points (e.g., meteorological stations) (Gobakis et al., 2011; Kolokotroni et al., 2009; Santamouris et al., 1999). As a result, global models are commonly established to describe the overall relationships between various influencing factors and LST (Santamouris et al., 1999; Di et al., 2016; Benghanem et al., 2009; Afzali, 2011). Geographical variations of the relationships are neglected. In addition, the large quantities of remote sensing data are not utilized to their full potentials. Such models generally lead to unsatisfactory estimates at each specific location. Therefore, using large quantity of data obtained from remote sensing and considering spatial heterogeneity will likely improve the accuracy and robustness of the ANN or DNN models.

Although uncommon in UHI studies, hybrid approaches that combine the regression models and neural networks are also used to solve prediction or estimation problems. For example, Zhang (2003) proposed a hybrid approach to time series forecasting by combining autoregressive integrated moving average (ARIMA) models and neural network models (Zhang, 2003). Results suggest that using hybrid models or combining several models may be more effective and efficient in improving forecasting accuracy (Makridakis, 1989). The combination of GWR and neural networks has been successfully adopted in quantifying the spatiotemporal relationships in environmental pollution modeling (Wu et al., 2020) and housing price analysis (Hagenauer and Helbich, 2021). These studies show the potentials of using the hybrid models to handle complex spatial non-stationarity in various geographical processes and environmental phenomena. However, to our best knowledge, the application of such hybrid approaches to predicting urban thermal environment has not been reported.

Urban form and function vary greatly (Živković, 2020). Innovative modeling approaches are needed to capture spatial

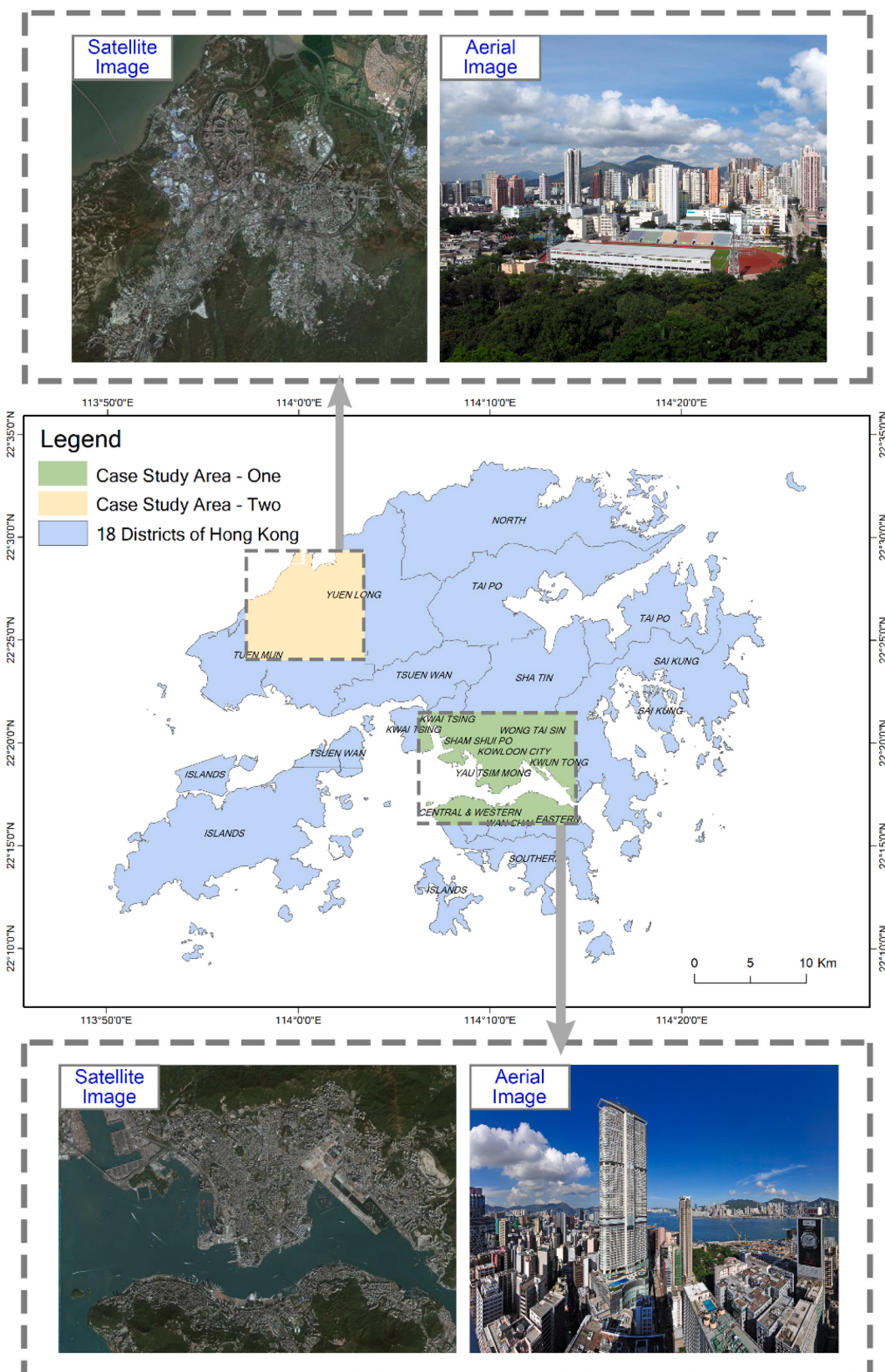


Fig. 1. Locations of the two representative regions.

heterogeneity and a large number of underlying factors that may also interact with each other. Based on the discussions above, this study attempts to develop a model to more accurately estimate LST by: (1) taking advantages of the wide coverage of remote sensing data, (2) considering spatial heterogeneity of the relationship between LST and various influencing factors, and (3) accommodating the nonlinear relationships between LST and the influencing factors and the interactions between the influencing factors. Such model is also compared with traditional approaches to estimating LST, including OLS, GWR, neural network models. A better model will enable us to more accurately predict LST in a specific location, but more importantly, it helps identify strategies to improve urban thermal environment through revealing the quantitative contributions of the underlying factors to LST. The following specific objectives are put forward:

- (1) The development of an integrated (hybrid) DNN and GWR model, along with the conventional OLS, GWR, and DNN models, to estimate LST using a variety of data from five categories, including: LULC composition and surface characteristics, LULC configuration, urban forms, anthropogenic activities, location and local climate.
- (2) Performance comparison of the hybrid model with the traditional ones (OLS, GWR, and DNN) based on a large quantity of test data (155,728 data points in total) and a long time period (2016–2019) in representative regions in Hong Kong.
- (3) The identification of major contributing factors to LST from the sixteen explanatory variables through attribution analysis and the recommendation of possible strategies for UHI mitigation.

## 2. Methodology

### 2.1. Study area

This research was conducted in two representative regions of Hong Kong (Fig. 1). Study area one is located in the Kowloon Peninsula. Study area two is situated in Tin Shui Wai, Tuen Mun, and Yuen Long of the New Territories. The landscapes of both study areas are dominated by built-up land, green space (woodland, shrubland, grassland), and exposed impervious surfaces. According to the local climate zone (LCZ) classification system (Stewart and Oke, 2012; Zheng et al., 2018; Wang et al., 2018), the built type of study area one mainly consists of LCZ 1 (compact high-rise buildings) and LCZ 4 (open high-rise buildings), while the built type of study area two mostly includes LCZ 3 (compact low-rise buildings) and LCZ 9 (sparsely built buildings). Detailed information of both study areas is presented in Table 1.

According to the major LCZs and LULC types shown in Table 1, the two study areas differ significantly in land surface properties, land use patterns, and urban morphology. Study area one is the city center, dominated by compact high-rise buildings and paved surfaces. Study area two is located in sub-urban regions, commonly characterized by low-rise or sparse buildings and relatively abundant greenery. These two areas represent typical yet different urban development patterns in Hong Kong. Therefore, the selection of these two study areas for model development and validation can make the model more robust and representative.

### 2.2. Data source

Spatial data in the GIS format was obtained from the Planning Department of Hong Kong, including the building coverage and height, coverage of transport infrastructures (road and transport facilities, railways). Demographic data was obtained from 2016 Hong Kong census data available on the Census and Statistics Department, including population in the year of 2016 and projected population from 2017 to 2019 in each district and tertiary planning unit (TPU).

A total of 20 remote sensing images from 2013 to 2020 were collected from the U.S. Geological Survey (USGS) (<https://earthexplorer.usgs.gov/>). Sixteen Landsat images covering two representative areas were selected to retrieve LST information at different time points. Four Sentinel images covering the entire Hong Kong were selected to represent the LULC characteristics of each studied year (2016–2019). All the used imagery data is summarized in Table 2.

**Table 1**

Detailed information of the two study areas.

	Study area one (Kowloon Peninsula)	Study area two (Tin Shui Wai, Tuen Mun, and Yuen Long)
Area (km <sup>2</sup> )	105.00	89.66
Percentage of major built types in LCZs <sup>1</sup>	LCZ 1: 28% LCZ 4: 15% LCZ 3: 5%	LCZ 3: 14% LCZ 9: 14% LCZ 4: 12% LCZ 6: 7%
Percentage of LULC types	Built-up lands: 32% Exposed impervious surfaces: 34% Greenery: 34%	Built-up lands: 38% Exposed impervious surfaces: 17% Greenery: 45%
Population density (persons/km <sup>2</sup> )	37,674	8110

Note: <sup>1</sup>LCZ classification refers to the research of Stewart and Oke (2012) (Stewart and Oke, 2012).

**Table 2**

A summary of all the used imagery data.

Year	Imagery ID	Path Row	Date of acquisition	Resolution (m)
Landsat 8 OLI/TIRS imagery				
Study area one				
2016	LC81210452016143LGN01	121/045	22/05/2016	30
2016	LC81210452016239LGN01	121/045	26/08/2016	30
2017	LC81210452017049LGN00	121/045	18/02/2017	30
2017	LC81220442017296LGN00	122/044	23/10/2017	30
2018	LC81220442018011LGN00	122/044	11/01/2018	30
2018	LC81220452018091LGN00	122/045	01/04/2018	30
2019	LC81210452019263LGN00	121/045	20/09/2019	30
2019	LC81220452019334LGN00	122/045	30/11/2019	30
Study area two				
2013	LC81220442013221LGN01	122/044	09/08/2013	30
2016	LC81220442016038LGN01	122/044	07/02/2016	30
2016	LC81220442016086LGN01	122/044	26/03/2016	30
2016	LC81220442016262LGN01	122/044	18/09/2016	30
2017	LC81220442017296LGN00	122/044	23/10/2017	30
2018	LC81220442018011LGN00	122/044	11/01/2018	30
2019	LC81220442019318LGN00	122/044	14/11/2019	30
2020	LC81220442020049LGN00	122/044	18/02/2020	30
Sentinel 2 imagery				
Study area one & two				
2016	L1C_T49QHE_A007751_20161216T031127	T49QHE	2016/12/16	10
2017	L1C_T49QHE_A013185_20171231T031020	T49QHE	2017/12/31	10
2018	L1C_T49QHE_A018333_20181226T030713	T49QHE	2018/12/26	10
2019	L1C_T49QHE_A023338_20191211T030708	T49QHE	2019/12/11	10

\* Due to the lack of available imagery of study area two during 2016–2020, two additional imageries which collected on Aug. 09th of 2013 and Feb. 18th of 2020 were used.

### 2.3. Development of indices

#### 2.3.1. Retrieval of LST and dependent variable

The study areas were divided into analysis grids of 100 m by 100 m. The average LST within each grid was used as the dependent variable. The LST data was derived from cloud-free Landsat 8 thermal infrared sensor (TIRS) images.

Before the retrieval of LST, the self-adaptive filter method was applied to the DN values for noise reduction. Then, the single-channel algorithm was used to retrieve LST from Landsat 8 TIRS band 10 images. The procedure has been widely applied in existing studies (Jia and Wang, 2020; Chen et al., 2006; Bendib et al., 2017; Yin et al., 2018b). Firstly, radiometric and geometrical distortion was corrected. Secondly, the corrected digital number (DN) values were converted to the top of atmosphere (TOA) spectral radiance using the radiance rescaling factor. Thirdly, the TOA brightness temperature was computed from TOA spectral radiance using the thermal conversion coefficients which are band-specific constants provided in the Landsat product metadata file. Finally, LST was calculated from the TOA brightness temperature, the wavelength of emitted radiance, and land surface emissivity (LSE). LSE is the average emissivity of an element on the earth surface. It is commonly estimated from the normalization differential vegetation index (NDVI). LST maps were finally created for each dataset at the resolution of 100 m.

#### 2.3.2. Explanatory variables

Urban thermal environment is affected by a large number of factors and their interactions. Overall, the potential influencing factors were divided into five categories: (1) LULC composition and surface characteristics, (2) LULC configuration, (3) urban form, (4) anthropogenic activities, and (5) location and local climate. Fig. 2 displays all the explanatory variables used in this paper.

Several factors are placed under LULC composition and surface characteristics. Impervious surface and scarcity of greenery result in increases in solar energy absorption, heat trapping, and reduction in evapotranspiration (Wong et al., 2021), leading to UHI effect (Li et al., 2011; Li et al., 2017). Therefore, the fractions of areas covered by built-up lands ( $P_{built}$ ), roads ( $P_{road}$ ), exposed impervious surfaces (e.g., rock formation, parking lots, represented by  $P_{exposed}$ ), and greenery ( $P_{green}$ ) were chosen as explanatory variables. These indices were computed as the proportion of each LULC type within every analysis grid (at the resolution of 100 m) divided by the total grid area. Of the variables,  $P_{exposed}$ ,  $P_{built}$  and  $P_{green}$  were identified from the raster layers of LULC patterns derived from the Sentinel 2 imagery. Supervised maximum likelihood classification was performed to identify the LULC patterns. The training sites were selected in agreement with the satellite image and Google Earth.  $P_{road}$  was identified from the vectorized road layer of the open street map (OSM). Greenery can cool the surrounding environment through shading and evapotranspiration, but the area fraction of greenery may not well reflect the intensity of greenery. Therefore, leaf area index (LAI), defined as the total one-sided area of leaf tissue per unit ground surface area (Kolokotsa et al., 2013; Chen and Black, 1992), was selected to represent the cooling effect of greenery intensity.

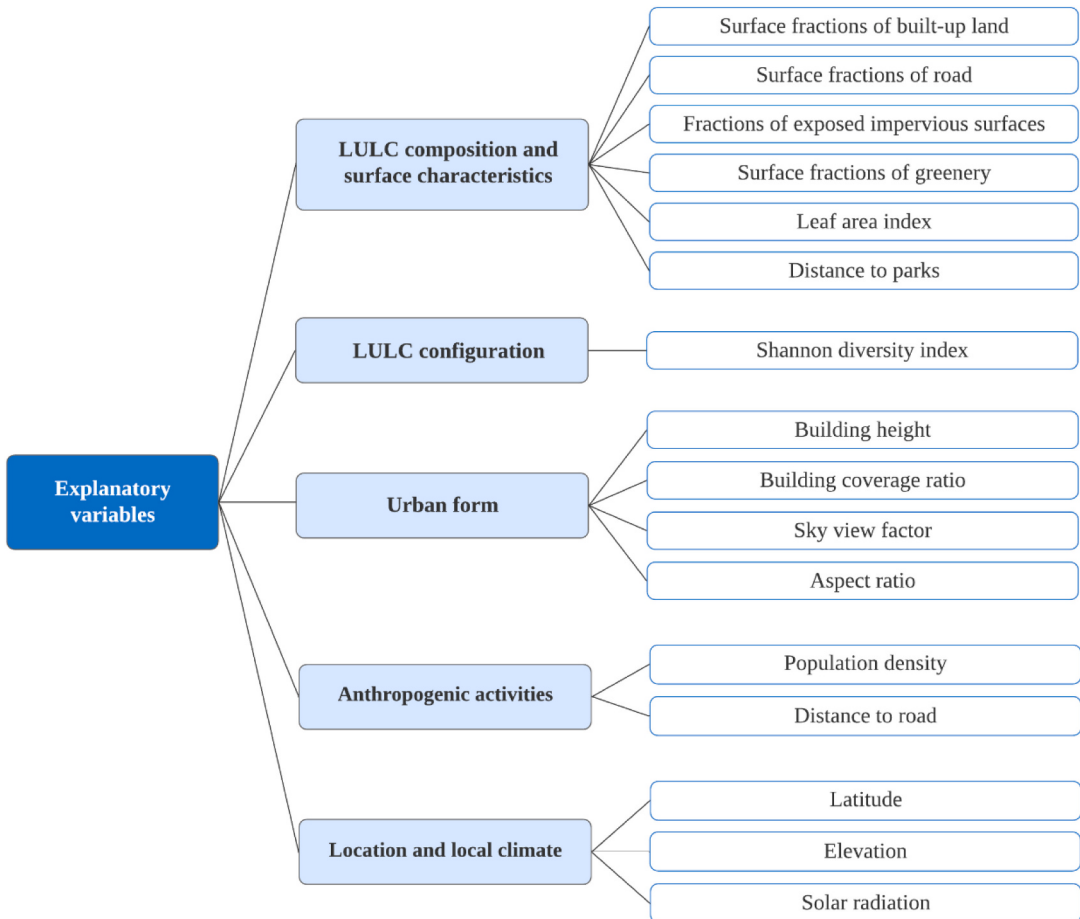


**Fig. 2.** The explanatory variables.

LAI values were estimated based on the nonlinear relationship between NDVI and LAI in urban areas (Ren et al., 2017). In addition, even though a modelled land parcel may not directly have vegetation, if it is close to a large vegetated area that has cool air, LST of the parcel may be reduced. Therefore, distance to large vegetated areas or parks ( $D_{park}$ ) was selected as an explanatory variable. The locations of large vegetated areas or parks were identified from the land utilization map of Hong Kong. Straight-line distances from each analysis grid center to the large urban parks ( $D_{park}$ ) were calculated using the proximity analysis tool in ArcGIS 10.2.

LULC configuration is represented by the Shannon diversity index (SHDI). Previous studies found that landscape pattern affects UHI through the spatial arrangement, position, and orientation of landscape units (i.e., patches) within each class or landscape type (Li et al., 2011; Li et al., 2017). SHDI is a general index to measure landscape diversity. This index refers to the variety and abundance of different land cover types within a landscape (Ramezani, 2012). A higher SHDI value indicates higher patch richness and more staggered landscape distribution pattern (Xie et al., 2013), while a lower value indicates that the landscape is less diversified.

LST is also related to urban form (Yin et al., 2018b; Yang and Li, 2015). Urban form affects shortwave radiation from the sun, radiative heat loss at night, and wind flow pattern (Lin et al., 2017). Relationships between urban form and LST variations were explored in several empirical studies using urban form indices such as building height (BH), building coverage ratio (BCR), sky view factor (SVF), and aspect ratio (AR) (Yin et al., 2018b; Guo et al., 2020; Sun et al., 2019). In this study, BH and BCR were directly derived from the OSM layer. SVF is defined as the ratio of radiation received by a planar surface from the sky to that received from the entire hemispheric radiating environment (Scarano and Mancini, 2017; Watson and Johnson, 1987). Higher values of SVF correspond to flatter and less obstructed surfaces, while lower values imply more confined, scattered and denser areas (Scarano and Sobrino, 2015). AR is defined as the ratio of building height to width of a street canyon. A 5-m digital surface model (DSM) of Hong Kong, which contains elevation information of both natural features and man-made features, was used for SVF and AR calculations. The SVF calculation tool – SAGA GIS (Conrad et al., 2015) and the aggregation tool in ArcGIS 10.2 were applied to generate the mean SVF value of each grid. However, due to the complex geometry of the street, there is no standardized method to calculate AR in Hong Kong (Zheng et al., 2018; HKBuildingDepartment, 2009). This study adopted the calculation procedures introduced by Hong Kong sustainable building design guidelines (HKBuildingDepartment, 2009). The mean AR value of each grid was computed by using the area-weighted mean building height divided by the mean street width.

Two factors are included under the category of anthropogenic activities. Anthropogenic heat may be subdivided into three components: heat produced by combustion of vehicle fuels, heat released from “stationary sources” (primary within buildings), and heat released by metabolism (ASHRAE, 2005; Grimmond, 1992). Heat owing to human activities was shown to be related to population density (*PopD*) (Dong et al., 2017). Distance to road ( $D_{road}$ ) was also used to represent heat released from vehicular traffic.  $D_{road}$  can be measured from the OSM layer using the proximity analysis tool. However, quantitative analysis of the effects of *PopD* on LST was usually hampered by the problem of spatial unit difference (Yuan et al., 1997). To solve this problem, the estimation of grid-based *PopD* value followed the procedure developed by Yuan et al. (Yuan et al., 1997). The model describes the relationship between population and LULC pattern:

$$y_i = \sum_{j=1}^n (b_j x_{ij} + \varepsilon_i) \quad (1)$$

where  $y_i$  is the total population count for the  $i^{\text{th}}$  tertiary planning unit (TPU) and  $x_{ij}$  is the total area for the  $j^{\text{th}}$  land cover type within the  $i^{\text{th}}$  TPU. *PopD* within a TPU is not homogeneous but may be driven by the LULC composition and configuration (Xiao et al., 2008; Yuan et al., 1997; Flowerdew and Green, 1989). Therefore, the estimate ( $b_j$ ) on population density for each land cover type within the whole study area was firstly evaluated by Eq. (1) under the condition that  $i \geq j$ . Then,  $b_j$  was refined to describe the population density of each land cover type within TPUs using the following equations:

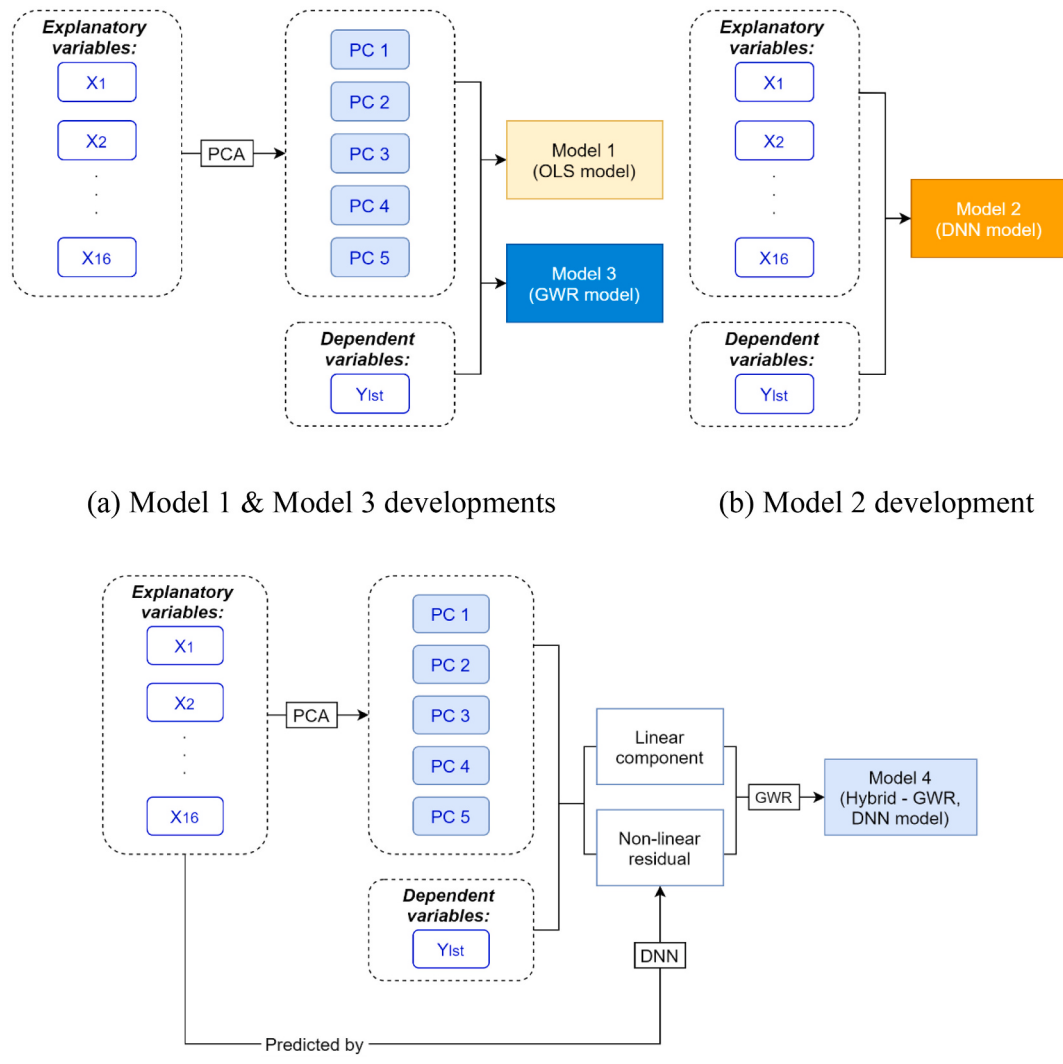


**Fig. 3.** The process of model developments.

$$p_i = \sum_{j=1}^n (b_j x_{ij}) \quad (2)$$

$$b_{ij} = \frac{y_i}{p_i} b_j \quad (3)$$

where  $p_i$  is the predicted population count for the  $i^{\text{th}}$  TPU, and  $b_{ij}$  is the refined population density for the  $j^{\text{th}}$  land cover type within the  $i^{\text{th}}$  TPU. After scaling, the sum of the refined population density ( $b_{ij}$ ) multiplying  $x_{ij}$  within the  $i^{\text{th}}$  TPU can be mathematically proven to be equal to the population counts ( $y_i$ ), as shown in Eq. (4). For each analysis grid within the  $i^{\text{th}}$  TPU, the population is expressed in Eq. (5).

$$y_i = \sum_{j=1}^n (b_{ij} x_{ij}) \quad (4)$$

$$Q_k = \sum_{k=1}^n (b_{kj} A_{kj}) \quad (5)$$

where  $Q_k$  is the total population count for the  $k^{\text{th}}$  grid, and  $A_{kj}$  is the area for the  $j^{\text{th}}$  land cover type within the  $k^{\text{th}}$  grid. Hence, the grid-based  $\text{PopD}$  values were estimated based on the relationship between population and LULC pattern.

The last category is about location and local climate, which include latitude (LAT), elevation (EL), and solar radiation (RD) information. LAT and EL were obtained from the digital elevation model (DEM) of Hong Kong, while RD was computed using the area solar radiation tool in ArcGIS 10.2. This tool provides an output of incoming solar radiation based on the hemispherical viewshed algorithm (Rich, 1990; Dubayah and Rich, 1995).

## 2.4. Model development

### 2.4.1. A general introduction to the model development process

The development processes of the four types of models are shown in Fig. 3. The extracted principal components from the 16 explanatory variables were used as inputs in model 1 (OLS) and model 3 (GWR). Model 2 was constructed using DNN based on all the explanatory variables. Model 4 was developed using a hybrid approach integrating both GWR and DNN. In model 4, the principal components were initially used as inputs for GWR, then the model residuals from the GWR were estimated by using DNN based on the 16 explanatory variables, and at last the linear and non-linear components were combined to estimate the LST.

### 2.4.2. Principal component analysis and linear regression

Multicollinearity between explanatory variables may prevent the OLS and GWR models from reaching correct solutions. In order to remove multicollinearity, principal component analysis (PCA) was performed before OLS and GWR analysis. PCA is widely used for dimension reduction and feature extraction (Jhajharia et al., 2016). The principal components with an eigenvalue greater than one were selected as the inputs of the OLS and GWR models.

The OLS regression model is expressed as:

$$y_i = \beta_0 + \sum_{j=1}^k \beta_j x_{ij} + \varepsilon_i \quad (6)$$

where  $y_i$  is the  $i^{\text{th}}$  observation of the dependent variable,  $x_{ij}$  is the  $i^{\text{th}}$  observation of the  $j^{\text{th}}$  principal components,  $\beta_j$  is the regression coefficient of the  $j^{\text{th}}$  variable, and  $\varepsilon_i$  is the error term. In Eq. (6), neither  $\beta_0$  nor  $\beta_j$  varies spatially.

The GWR model extends the conventional regression methods by enabling spatial variations of regression coefficients, as shown in the following equation (Brunsdon et al., 1996; Matthews and Yang, 2012):

$$y_i = \beta_{i0} + \sum_{j=1}^k \beta_{ij} x_{ij} + \varepsilon_i \quad (7)$$

where  $\beta_{i0}$  and  $\beta_{ij}$  vary spatially based on local estimates while all the other parameters are the same as those in Eq. (6).

### 2.4.3. The hybrid approach

The hybrid approach developed in this study follows the method proposed by Zhang (Zhang, 2003). The method was originally used for time series forecasting of sunspot activities. The relationship between the linear and non-linear components takes the following form (Zhang, 2003; Alalawi et al., 2008):

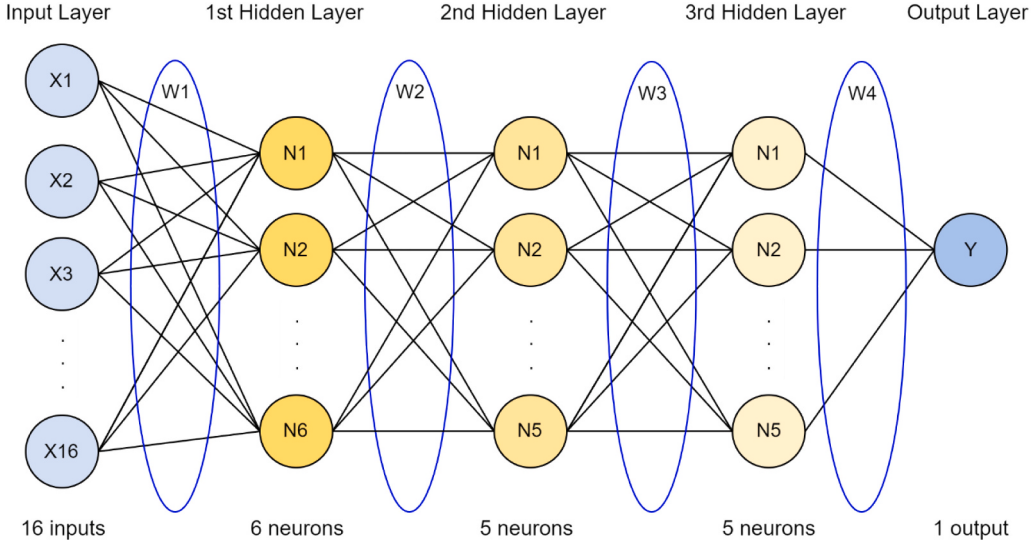
$$y_i = G_i + N_i \quad (8)$$

$$e_i = y_i - \hat{G}_i \quad (9)$$

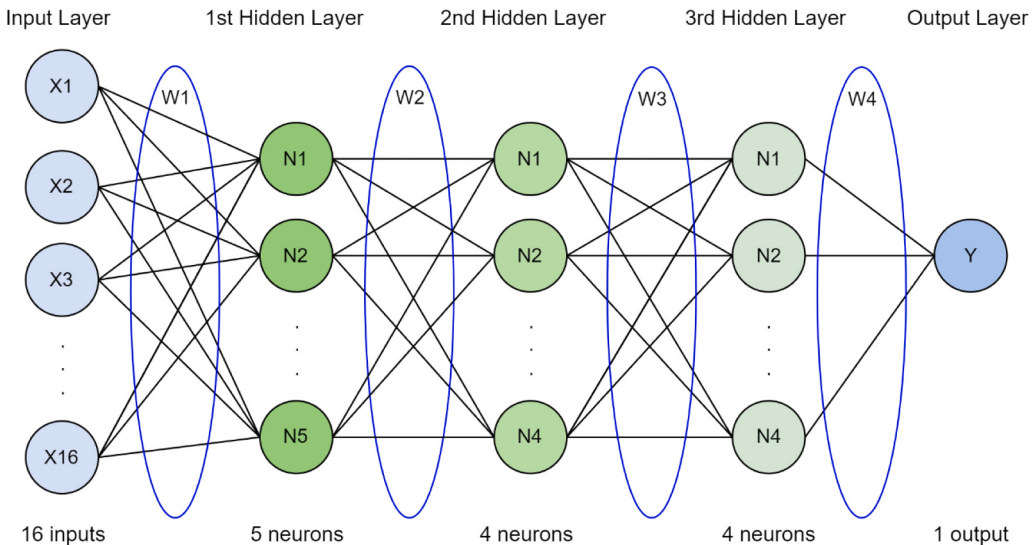
where  $y_i$  is the observed value at the location  $i$ ,  $G_i$  and  $N_i$  are the linear and non-linear components of the explanatory variables at the location  $i$ , respectively, and  $e_i$  is the difference between the observed value and the estimated linear component ( $\hat{G}_i$ ) by the GWR model. In this study,  $\hat{G}_i$  was estimated using the principal components. The residual ( $e_i$ ) from the GWR model was further estimated using DNN as expressed in Eq. (10):

$$e_i = f(x_{i1}, x_{i2}, \dots, x_{in}) + \varepsilon_i \quad (10)$$

where  $f(x_{i1}, x_{i2}, \dots, x_{in})$  is the non-linear function for  $e_i$  captured by DNN,  $x_{ij}$  ( $1 \leq j \leq n, n = 16$ ) is the  $i^{\text{th}}$  observation of the  $j^{\text{th}}$  explanatory variable, and  $\varepsilon_i$  is the prediction error term. The combination of the estimated linear component ( $\hat{G}_i$ ) and the non-linear component ( $\hat{N}_i$ ) for the location  $i$  can be expressed as:



(a)



(b)

**Fig. 4.** The chosen DNN structures (a: study area one; b: study area two).

$$\hat{y}_i = \hat{G}_i + \hat{N}_i = \beta_{i0} + \sum_{j=1}^k \beta_{ij} x_{ij} + \beta_{ie} \hat{e}_i + \varepsilon_i \quad (11)$$

where  $\hat{e}_i$  is the predicted residual term by DNN, and  $\beta_{ie}$  is the coefficient of the residual term for the location  $i$ .

#### 2.4.4. The DNN structure

As compared with conventional ANN, DNN contains more hidden layers and nodes, making it better to simulate the human neural system. The DNN model was constructed and trained using TensorFlow (Abadi et al., 2016). During the training process, the learning rate was set to 0.001, and the maximum number of epochs was 1000. Two additional Landsat images from representative area one and area two (acquired on 04/02/2021 and 20/02/2021, respectively) were used to determine the DNN structure. Different DNN structures were tried and the DNN with three hidden layers was found to provide the best performance. The final determined DNN structure used in model 2 and model 4 is shown in Fig. 4, which consists of 16 neurons in the input layer (corresponding to those 16 explanatory variables) and three hidden layers with 6, 5, and 5 neurons for study area one, and 5, 4, and 4 neurons for study area two, respectively. The simulated results and the observations of the two datasets are shown Fig. 5. The regression coefficients for the two datasets are both close to one (at 0.9835 in study area one and 0.9691 in study area two), and the mean squared errors (MSEs) are 0.75 °C and 1.08 °C, respectively. Therefore, the chosen DNN structure and coefficients can well predict the LSTs. The same structure was adopted for the subsequent analysis using model 4, although the coefficients varied in each of the 16 dataset. In each dataset, 70% of the observations were randomly picked as training samples, while the remaining 30% were used to evaluate the fitness of the models.

### 3. Results and discussion

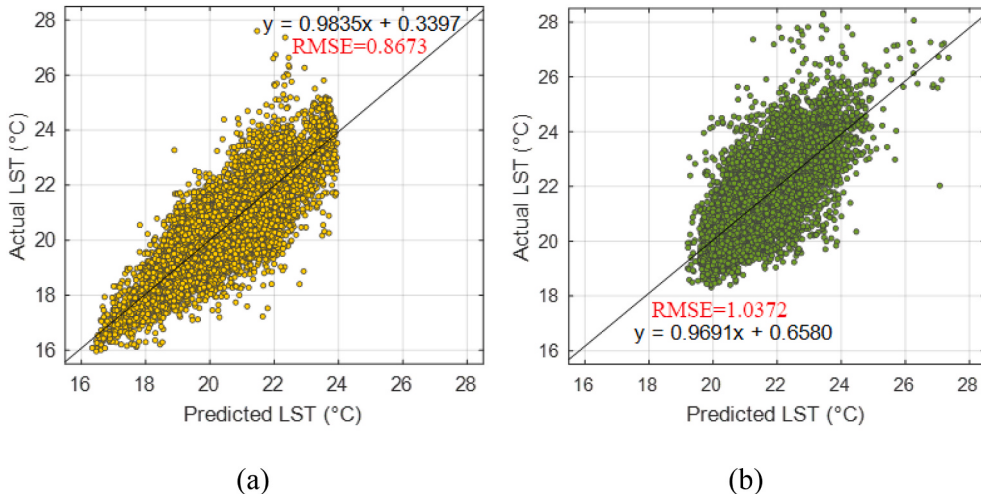
#### 3.1. Model performance in LST estimation

Through principal component analysis (PCA), the first five principal components with an eigenvalue greater than one were extracted. These principal components explain 66.50% of the total variation in study area one and 57.68% of the total variation in study area two. As introduced before, the principal components were used as inputs for model 1, 3, and 4. MSE and the coefficient of determination ( $R^2$ ) were used to evaluate and compare the performance of the models.

Table 3 displays the overall model performance in study areas one and two. The detailed results for each dataset in study area one, which consists of 10,500 analysis grids, are summarized in Table A1 of the Supplementary Material, while the results for each dataset in study area two (8966 grids in total) are presented in Table A2.

For study area one, a consistent pattern in MSE and  $R^2$  can be found from the eight datasets. Compared to the traditional OLS model (model 1), model 2 using DNN, model 3 using GWR, and model 4 integrating GWR and DNN all showed better performance. Particularly, the hybrid model (model 4) performed the best with the least MSE (ranging from 0.260 to 0.636 °C in study area one and 0.483 to 1.017 in study area two) and the highest  $R^2$  (ranging from 0.767 to 0.910 in study area one and 0.651 to 0.777 in study area two). A comparison of the  $R^2$  values of the four models in the two study areas is shown in Fig. 6.

Fig. 6 indicates that, as compared to the OLS model, improvements on estimation performance were achieved in models using DNN and GWR. Compared to the models in study area one (Fig. 6 (a)), improvements on  $R^2$  values for model 4 in study area two (Fig. 6 (b)) are even more significant. In study area one, the performance of model 4 improves 54.1%, 7.2%, and 8.1% than the performance of

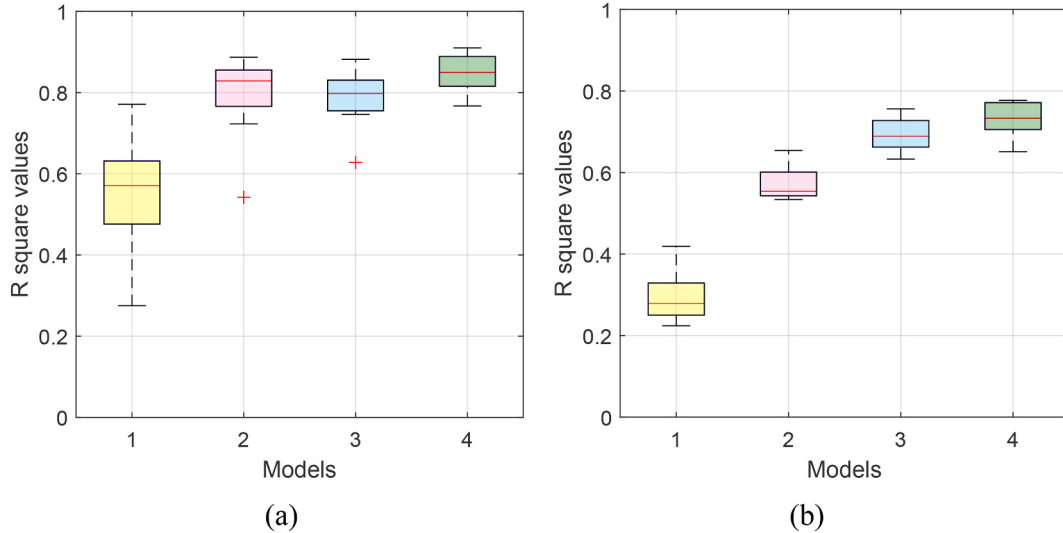


**Fig. 5.** Regressions between DNN outputs and observed values (a: study area one; b: study area two).

**Table 3**

Overall model performance in study areas one and two.

	Study area one		Study area two		Area-weighted average	
	MSE	R <sup>2</sup>	MSE	R <sup>2</sup>	MSE	R <sup>2</sup>
Model 1	1.40	0.55	1.88	0.29	1.62	0.43
Model 2	0.70	0.79	1.11	0.57	0.89	0.69
Model 3	0.73	0.78	0.81	0.69	0.76	0.74
Model 4	0.52	0.85	0.70	0.73	0.60	0.79

**Fig. 6.** The R<sup>2</sup> of the models for all the datasets in study areas one (a) and two (b).

models 1 to 3, respectively in terms of the averaged R<sup>2</sup>; while in study area two, the improvements are 147.9%, 27.6%, and 5.4%, respectively. The high R<sup>2</sup> value of the hybrid model indicates that the majority of the variations in the data can be captured by this model. The results indicate that the hybrid DNN model is a powerful approach to capture the geographically heterogeneous and nonlinear relationships between various explanatory variables and LSTs. Note that model 3 and model 4 also provide the spatial pattern of the local R<sup>2</sup>, which are displayed in Figs. A1-A2 of the Supplementary Material. In addition, model 4 outperforms model 3 among all the datasets, suggesting that the combination of GWR and DNN indeed leads to the improvement of estimation accuracy. The spatial patterns of estimation performance of model 3 and model 4 of datasets with the highest R<sup>2</sup> in two regions (study areas one: dataset 7 (acquired on 2019.09.20); study area two: dataset 4 (acquired on 2016.09.18)) are shown in Fig. 7.

On the same image, estimation accuracy varies with locations. As shown in Fig. 7 (a) and (b), satisfactory R<sup>2</sup> is observed in most regions, including the forestry (e.g., the northern regions in study area one), commercial built-up (e.g., Hong Kong Island - the southern regions in study area one), and residential built-up areas (e.g., the middle regions in study area two). The regions generally associated with low R<sup>2</sup> values in study areas one and two are marked in circles. In Fig. 7 (a), this region is a built-up area close to the mountain forests with geographical features not similar to other regions. The estimation accuracy is also relatively low in coastal areas. According to literature, differences in surface roughness over water versus land areas result in a strong and unstable air mass near the coast (Smith, 1988). Consequently, the heat island formation is suppressed in this area (Doick et al., 2014). In Fig. 7 (b), the overall estimation accuracy of both model 3 and model 4 in study area two is slightly deteriorated as compared to the model performance in study area one. The northern coastal regions where wetlands are abundant are always associated with low estimation accuracy. This may be caused by waterbodies that are not included as an explanatory variable.

The estimation accuracy varies between images taken at different dates. The estimation accuracy of the hybrid model is generally higher in warm seasons (e.g., study area one: R<sup>2</sup> = 0.910 in dataset 7 (Sep. 20th), R<sup>2</sup> = 0.892 in dataset 2 (Aug. 26th); study area two: R<sup>2</sup> = 0.777 in dataset 4 (Sep. 18th), R<sup>2</sup> = 0.776 in dataset 5 (Oct. 23rd)). However, the most remarkable improvement using the hybrid model usually appears in winter. Compared to the performance of model 1, the R<sup>2</sup> of model 4 improved significantly in dataset 3 (Feb. 18th) of study area one in dataset 6 (Jan. 11th) of study area two at 52.10% and 50.30%, respectively. Results indicate that the employed explanatory variables better characterize the urban temperature pattern in warm seasons, while in cold seasons, the relationship between LST and the explanatory variables may not be straightforward. In this case, the application of the hybrid approach can significantly improve the model performance.

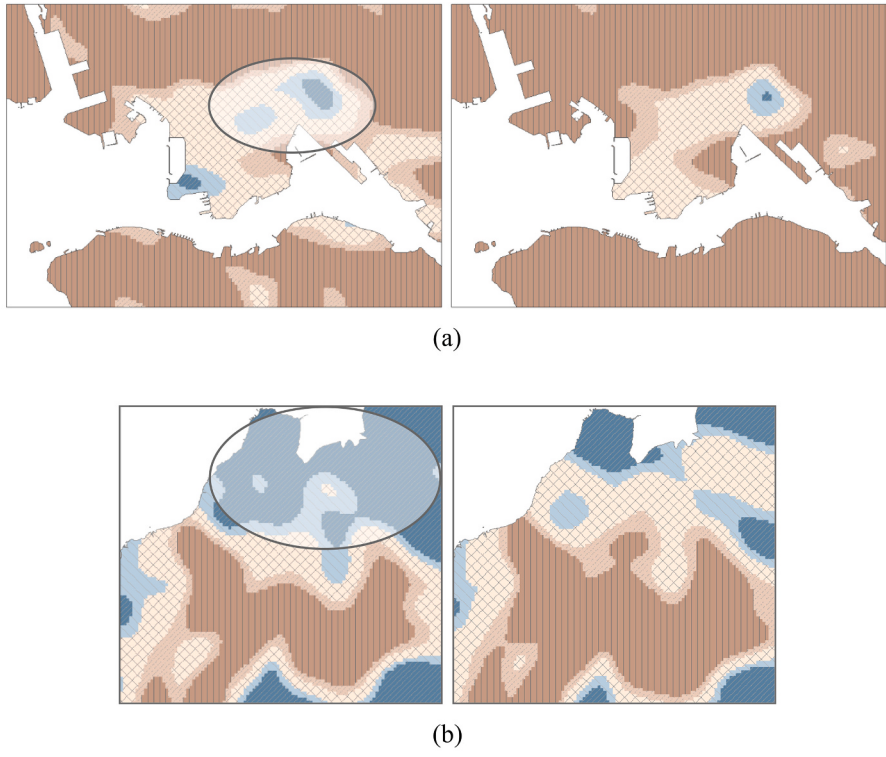


**Fig. 7.** The spatial patterns of estimation performance of model 3 and model 4 in datasets with the highest  $R^2$  in study areas one (a) and two (b).

### 3.2. The identification of leading factors affecting LST

The LST estimation results introduced above suggest that the explanatory variables can generally well explain variations in LST of the study areas, and model 4 performs the best. Based on model 4, a sensitivity analysis was conducted by systematically changing the value of each explanatory variable and assessing the impact on the resulted LST. The sensitivity of LST against each normalized

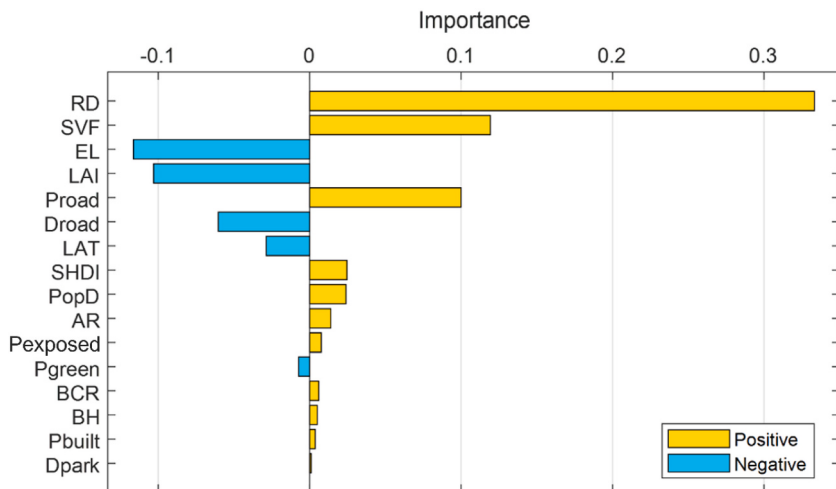


**Fig. 8.** The importance of explanatory variables in both study areas.

(Note: RD: solar radiation; SVF: sky view factor; EL: elevation; LAI: leaf area index;  $P_{road}$ : the fraction of roads;  $D_{road}$ : distance to roads; LAT: the latitude; SHDI: the Shannon diversity index;  $PopD$ : the population density; AR: the aspect ratio;  $P_{exposed}$ : the fraction of exposed impervious surfaces;  $P_{green}$ : the fraction of greenery; BCR: the building coverage ratio; BH: the building height;  $P_{built}$ : the fraction of built-up land;  $D_{park}$ : distance to parks.)

explanatory variable is shown in Fig. 8.

The signs of the sensitivity analysis results in Fig. 8 appear to be reasonable. LST is the most sensitive to solar radiation (RD). This is understandable as solar radiation is the driving factor for temperature increase. Besides RD, LST is also very sensitive to sky view factor (SVF), elevation (EL), leaf area index (LAI), the surface fraction of roads ( $P_{road}$ ), and distance to roads ( $D_{road}$ ). Similar influencing factors are also reported in literature (Yin et al., 2018b; Scarano and Mancini, 2017; Oke, 2002; Chen et al., 2014). Overall, the sky view factor is positively related to LST. This can be explained by the excessive sky exposure and solar radiation due to the lack of the obstruction effects by tall buildings, plants, or narrow streets (Scarano and Sobrino, 2015; Oke, 1981; Zhang et al., 2019). As expected, LST is negatively related to elevation. LST is also negatively related to the leaf area index. In Hong Kong's subtropical climate, the intensity of vegetation apparently plays an important and beneficial role in reducing LST in urban areas. LST is positively related to the coverage of road. As more than 80% of the roads in Hong Kong are paved with asphalt which has low albedo value, roads are more likely to absorb solar light, causing temperature increase on road surface. In addition, vehicular traffic may also generate heat on roads. Conversely, increasing distance to roads is negatively related to LST because road traffic plays a major role of heat source in the studied areas. As compared to the top six factors, the effects of other factors on LST are relatively weak.

Fig. 9 shows the spatial patterns of the coefficients of two major influencing factors that are related to city planning: SVF and LAI. The coefficient variations in dataset 7 (acquired on 2019.09.20) from study area one and dataset 4 (acquired on 2016.09.18) from study area two are chosen to be displayed due to high fitness of the hybrid model.

Fig. 9 (a) suggests that the influence of SVF on LST varies greatly in the two study areas, even though it is overall positively related to LST. Study area one is characterized by relatively smooth terrain and high-rise, high-density development. In study area one, LST appears to be more sensitive to SVF in regions away from the coastal areas, where LST is likely more affected by waterbody and wind. In addition, the orientation of the buildings may determine the sensitivity of LST to SVF. The terrain of area two is rougher than that in study area one, and high-density built-up region is mixed with rural areas. Variations in elevation may affect the sensitivity of LST to SVF in area two, too. An upper-left and middle region in area two (blue color in the figure) is associated with high coefficients of SVF. This region is the major built-up area (Tin Shui Wai) with high-rise residential buildings, while the other regions are more rural. This suggests that SVF plays a very important role in determining LST in the high-rise built-up area as compared to the immediately

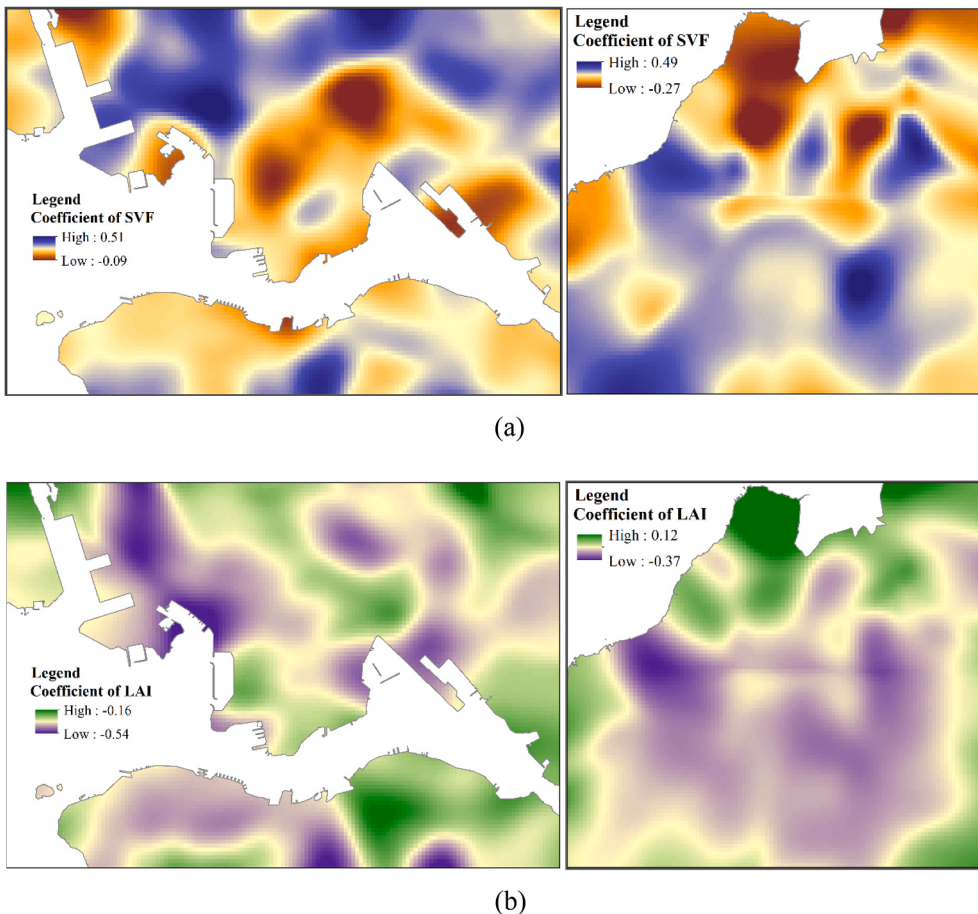


**Fig. 9.** The coefficient variations of SVF (a) and LAI (b) in two study areas.  
(Note: SVF: sky view factor; LAI: leaf area index)

neighboring rural area.

The sensitivity of LST to LAI also varies in the two study areas (see Fig. 9 (b)). In study area one, LST is the most sensitive to LAI in those heavily built-up areas with little existing vegetation such as regions near container terminals in Kwai Chung (upper-left) and CBD in Central, Hong Kong Island (lower-left). This implies that a slight increase in LAI in such areas may lead to a significant decrease in LST. In study area two, LST is also the most sensitive to LAI in those heavily built-up areas (Tin Shui Wai). In the north region of the study area two, however, LST becomes not sensitive to LAI. This is because the region already has high greenery density and also possesses abundant wetlands.

### 3.3. Discussion: Implications of the findings on urban development

As revealed in Fig. 8 and Fig. 9, land surface temperature (LST) in the two study areas is sensitive to a variety of factors, and the influences of these factors vary with geographical locations. Since LST is closely related to the urban heat island (UHI) effect—a major concern for high-density cities in hot climates such as Hong Kong, the findings above may assist decision-makers developing strategies to mitigate the UHI effect. Some of the possible strategies are discussed as follows.

- (1) LST is sensitive to urban forms such as sky view factor (SVF) and the aspect ratio (AR) of buildings. Overall, low SVF values caused by tall buildings and narrow streets can effectively increase shaded areas, thus keeping the bottom of urban canyons cooler than the surroundings (Elnahas, 2003). However, in certain regions especially coastal areas, decreasing the SVF value does not necessarily cause reduction in LST; other factors such as the sea breeze may become the dominant factor that affects the thermal environment (Sasaki et al., 2018; He et al., 2020). In such cases, decreasing the SVF value may be ineffective or even negatively affect the thermal environment (Guo et al., 2023; Chen et al., 2021; Gao et al., 2022). Therefore, urban forms need to be jointly considered with meteorological conditions in optimizing urban thermal environment.
- (2) LST is also closely related to LULC composition and surface characteristics. According to Fig. 8, a group of factors that represent impervious surfaces, including  $P_{road}$ ,  $D_{road}$ ,  $P_{exposed}$ , and  $P_{built}$ , have high influences on LST. In particular, LST is very sensitive to  $P_{road}$  (positively related) and  $D_{road}$  (negatively related). This implies that urban roads significantly contribute to UHI. Alternative construction materials such as those with high albedo or porous pavements may be considered in urban areas where UHI effect is a major concern.
- (3) Under LULC composition and surface characteristics, another group of factors that obviously affect LST is vegetation, including LAI and  $P_{green}$ . According to Fig. 8, both factors are negatively related to LST. Introducing green in urban areas helps reduce LST. As compared to green coverage, the intensity of the greening measures (as indicated by LAI) appears to have more obvious effect. Therefore, when possible, cities may use large plants such as intensive green roof or street trees to improve thermal environment.
- (4) Several other factors also seemingly affect LST. Both the Shannon diversity index (SHDI) and population density ( $PopD$ ) are positively related to LST. SHDI represents the richness of LULC configuration, and more urbanized area generally corresponds to higher SHDI values. Similarly, population density in more urbanized area is also high. This implies that people living in inner city are more vulnerable to UHI, and more active measures may be directed toward such areas for improvement.

Although the analysis results provide some useful findings, limitation needs to be recognized. In this study, LST was derived from satellite images acquired around a fixed time (10:50 am). Consequently, time series of LST cannot be obtained and analyzed. In addition, the explanatory factors used in this study may not cover all those affecting LST, such as meteorological parameters (Doick et al., 2014; Du et al., 2016). Such limitations may be overcome when more site monitoring data become available in the future. In spite of the limitations, the high  $R^2$  values generated by the hybrid model suggest that the model captures the majority of the variations of LST at the selected time window in the study areas. Geographical variations of the coefficients of the explanatory variables also provide a clearer picture on how the effects of the variables change in different locations.

## 4. Summary and conclusion

Four different methods to estimate LST were used and compared, including the ordinary least squares (OLS) model, geographically weighted regression (GWR) model, deep neural network (DNN), and a hybrid technique that combines the GWR and DNN. LST was derived from satellite imageries. Sixteen explanatory variables were obtained from different sources and categorized into five groups, including (1) LULC composition and surface characteristics, (3) LULC configuration, (3) urban form, (4) anthropogenic activities, and (5) location and local climate. Two study areas in Hong Kong were selected for analysis. At the resolution of 100 m, a total of 155,728 pixels were analyzed during a four-year study period. The following conclusions are drawn from the study:

- (1) The hybrid approach that combines GWR and DNN provides the best performance in nearly all the datasets and also a reasonable explanation on the relationships between LST and the explanatory variables.
- (2) The influences of the explanatory variables on LST vary greatly with locations, and such variations need to be considered in developing UHI mitigation strategies.
- (3) LST is the most sensitive to sky view factor (SVF) except for solar radiation (RD). The effects of greenery and road on LST are also significant: LST is strongly and negatively related to leaf area index (LAI) and the distance to roads ( $D_{road}$ ); while strongly and positively related to the coverage of roads ( $P_{road}$ ).

Conclusion (3) may be specific to the chosen study areas. However, conclusions (1) and (2) may be well applied to other study areas. In particular, the hybrid approach may be applied in other studies to handle the complicated spatial non-stationarity problems in various geographical processes and environmental phenomena.

#### CRediT authorship contribution statement

**Jia Siqi:** Conceptualization, Methodology, Software, Validation, Formal analysis, Investigation, Resources, Data curation, Writing – original draft. **Wang Yuhong:** Conceptualization, Writing – review & editing, Supervision, Project administration. **Chen Ling:** Methodology, Writing – review & editing. **Bi Xiaowen:** Methodology, Writing – review & editing.

#### Declaration of Competing Interest

The authors declare that they have no known competing financial interests or personal relationships that could have appeared to influence the work reported in this paper.

#### Data availability

The authors are unable or have chosen not to specify which data has been used.

#### Acknowledgment

This paper is based on the research project (*E-PolyU502/16*) and (*R5007-18*) funded by the Research Grant Council (RGC) of Hong Kong Special Administrative Region Government. The research is part of the study entitled *Urban Nature Labs (UNaLab)*, funded by the European Commission (EC)'s Horizon 2020 Research Scheme, Hong Kong RGC and other research partners.

#### Appendix A. Supplementary data

Supplementary data to this article can be found online at <https://doi.org/10.1016/j.uclim.2022.101390>.

#### References

- Abadi, M., Agarwal, A., Barham, P., Brevdo, E., Chen, Z., Citro, C., Corrado, G.S., Davis, A., Dean, J., Devin, M., 2016. Tensorflow: Large-Scale Machine Learning on Heterogeneous Distributed Systems. arXiv preprint arXiv:1603.04467.
- Afzali, A.A.A.G.Z. Mahboubeh, 2011. Ambient Air Temperature Forecasting Using Artificial Neural Network Approach, International Conference on Environmental and Computer Science, 19.
- Alalawi, S., Abdulwahab, S., Bakheet, C., 2008. Combining principal component regression and artificial neural networks for more accurate predictions of ground-level ozone. Environ. Model. Softw. 23, 396–403.
- Alcoforado, M.J., Andrade, H., 2005. Nocturnal urban heat island in Lisbon (Portugal): main features and modelling attempts. Theor. Appl. Climatol. 84, 151–159.
- ASHRAE, 2005. Thermal Comfort Chapter, Fundamentals Volume of the ASHRAE Handbook.
- Bendib, A., Dridi, H., Kalla, M.I., 2017. Contribution of Landsat 8 data for the estimation of land surface temperature in Batna city, eastern Algeria. Geocarto Int. 32, 503–513.
- Benghanem, M., Mellit, A., Alamri, S., 2009. ANN-based modelling and estimation of daily global solar radiation data: a case study. Energy Convers. Manag. 50, 1644–1655.
- Brunsdon, C., Fotheringham, A.S., Charlton, M.E., 1996. Geographically weighted regression: a method for exploring spatial nonstationarity. Geogr. Anal. 28, 281–298.
- Chen, J., Black, T., 1992. Foliage area and architecture of plant canopies from sunfleck size distributions. Agric. For. Meteorol. 60, 249–266.
- Chen X.-L., Zhao, H.-M., Li, P.-X., Yin, Z.-Y., 2006. Remote sensing image-based analysis of the relationship between urban heat island and land use/cover changes. Remote Sens. Environ. 104, 133–146.
- Chen, A., Yao, L., Sun, R., Chen, L., 2014. How many metrics are required to identify the effects of the landscape pattern on land surface temperature? Ecol. Indic. 45, 424–433.
- Chen, Q., Cheng, Q., Chen, Y., Li, K., Wang, D., Cao, S., 2021. The influence of sky view factor on daytime and nighttime urban land surface temperature in different spatial-temporal scales: a case study of Beijing. Remote Sens. 13.
- Conrad, O., Bechtel, B., Bock, M., Dietrich, H., Fischer, E., Gerlitz, L., Wehberg, J., Wichmann, V., Böhner, J., 2015. System for Automated Geoscientific Analyses (SAGA) v. 2.1. 4, 8. Geoscientific Model Development Discussions.
- Deng, C., Wu, C., 2013. Examining the impacts of urban biophysical compositions on surface urban heat island: a spectral unmixing and thermal mixing approach. Remote Sens. Environ. 131, 262–274.
- Di, Q., Kourakis, P., Schwartz, J., 2016. A hybrid prediction model for PM2.5 mass and components using a chemical transport model and land use regression. Atmos. Environ. 131, 390–399.
- Doick, K.J., Peace, A., Hutchings, T.R., 2014. The role of one large greenspace in mitigating London's nocturnal urban heat island. Sci. Total Environ. 493, 662–671.
- Dong, Y., Varquez, A.C.G., Kanda, M., 2017. Global anthropogenic heat flux database with high spatial resolution. Atmos. Environ. 150, 276–294.
- Dong, Y., Ren, Z., Fu, Y., Hu, N., Guo, Y., Jia, G., He, X., 2022. Decrease in the residents' accessibility of summer cooling services due to green space loss in Chinese cities. Environ. Int. 158, 107002.
- Du, H., Wang, D., Wang, Y., Zhao, X., Qin, F., Jiang, H., Cai, Y., 2016. Influences of land cover types, meteorological conditions, anthropogenic heat and urban area on surface urban heat island in the Yangtze River Delta urban agglomeration. Sci. Total Environ. 571, 461–470.
- Du, Z., Wang, Z., Wu, S., Zhang, F., Liu, R., 2020. Geographically neural network weighted regression for the accurate estimation of spatial non-stationarity. Int. J. Geogr. Inf. Sci. 34, 1353–1377.
- Dubayah, R., Rich, P.M., 1995. Topographic solar radiation models for GIS. Int. J. Geogr. Inf. Syst. 9, 405–419.

- Elnahas, M.M., 2003. The effects of urban configuration on urban air temperatures. *Archit. Sci. Rev.* 46, 135–138.
- Fagan, B., 2008. The Great Warming: Climate Change and the Rise and Fall of Civilizations. Bloomsbury Publishing USA.
- Flowerdew, R., Green, M., 1989. Statistical methods for inference between incompatible zonal systems. *Accur. Spat. Databases* 239–247.
- Gao, Y., Zhao, J., Han, L., 2022. Exploring the spatial heterogeneity of urban heat island effect and its relationship to block morphology with the geographically weighted regression model. *Sustain. Cities Soc.* 76.
- Gardner, M.W., Dorling, S., 1998. Artificial neural networks (the multilayer perceptron)—a review of applications in the atmospheric sciences. *Atmos. Environ.* 32, 2627–2636.
- Gobakis, K., Kolokotsa, D., Synnefa, A., Saliari, M., Giannopoulou, K., Santamouris, M., 2011. Development of a model for urban heat island prediction using neural network techniques. *Sustain. Cities Soc.* 1, 104–115.
- Grimmond, C., 1992. The suburban energy balance: methodological considerations and results for a mid-latitude west coast city under winter and spring conditions. *Int. J. Climatol.* 12, 481–497.
- Guo, G., Wu, Z., Xiao, R., Chen, Y., Liu, X., Zhang, X., 2015. Impacts of urban biophysical composition on land surface temperature in urban heat island clusters. *Landsc. Urban Plan.* 135, 1–10.
- Guo, J., Han, G., Xie, Y., Cai, Z., Zhao, Y., 2020. Exploring the relationships between urban spatial form factors and land surface temperature in mountainous area: a case study in Chongqing city, China. *Sustain. Cities Soc.* 61.
- Guo, F., Zhao, J., Zhang, H., Dong, J., Zhu, P., Lau, S.S.Y., 2023. Effects of urban form on sea cooling capacity under the heatwave. *Sustain. Cities Soc.* 88.
- Hagenauer, J., Helbich, M., 2021. A geographically weighted artificial neural network. *Int. J. Geogr. Inf. Sci.* 1–21.
- He, B.-J., Ding, L., Prasad, D., 2020. Outdoor thermal environment of an open space under sea breeze: a mobile experience in a coastal city of Sydney, Australia. *Urban Clim.* 31.
- HKBuildingDepartment, 2009. Sustainable Building Design Guidelines: Practice Note for Authorized Persons, Registered Structural Engineers and Registered Geotechnical Engineers.
- Howard, L., 1818. The Climate of London, W. Phillips, Sold also by J. and A. Arch.
- Jhajharia, S., Varshney, H.K., Verma, S., Kumar, R., 2016. A neural network based breast cancer prognosis model with PCA processed features. In: International Conference on Advances in Computing, Communications and Informatics (ICACCI). IEEE, pp. 1896–1901.
- Jia, S., Wang, Y., 2020. Effects of land use and land cover pattern on urban temperature variations: a case study in Hong Kong. *Urban Clim.* 34.
- Ketterer, C., Matzarakis, A., 2015. Comparison of different methods for the assessment of the urban heat island in Stuttgart, Germany. *Int. J. Biometeorol.* 59, 1299–1309.
- Kim, Y.-H., Baik, J.-J., 2002. Maximum urban heat island intensity in Seoul. *J. Appl. Meteorol.* 41, 651–659.
- Kolokotroni, M., Zhang, Y., Giridharan, R., 2009. Heating and cooling degree day prediction within the London urban heat island area. *Build. Serv. Eng. Res. Technol.* 30, 183–202.
- Kolokotsa, D., Santamouris, M., Zerefos, S.C., 2013. Green and cool roofs' urban heat island mitigation potential in European climates for office buildings under free floating conditions. *Sol. Energy* 95, 118–130.
- Konopacki, S., Akbari, H., 2002. Energy Savings for Heat-Island Reduction Strategies in Chicago and Houston (Including Updates for Baton Rouge, Sacramento, and Salt Lake City).
- Kusaka, H., Chen, F., Tewari, M., Dudhia, J., Gill, D.O., Duda, M.G., Wang, W., Miya, Y., 2012. Numerical simulation of urban Heat Island effect by the WRF model with 4-km grid increment: an inter-comparison study between the urban canopy model and slab model. *J. Meteorol. Soc. Japan Ser. II* (90B), 33–45.
- Li, S., Zhao, Z., Miaomiao, X., Wang, Y., 2010. Investigating spatial non-stationary and scale-dependent relationships between urban surface temperature and environmental factors using geographically weighted regression. *Environ. Model. Softw.* 25, 1789–1800.
- Li, J., Song, C., Cao, L., Zhu, F., Meng, X., Wu, J., 2011. Impacts of landscape structure on surface urban heat islands: a case study of Shanghai, China. *Remote Sens. Environ.* 115, 3249–3263.
- Li, W., Cao, Q., Lang, K., Wu, J., 2017. Linking potential heat source and sink to urban heat island: heterogeneous effects of landscape pattern on land surface temperature. *Sci. Total Environ.* 586, 457–465.
- Lin, P., Gou, Z., Lau, S., Qin, H., 2017. The impact of Urban Design descriptors on outdoor thermal environment: a literature review. *Energies* 10.
- Liu, W., Wang, Z., Liu, X., Zeng, N., Liu, Y., Alsaadi, F.E., 2017. A survey of deep neural network architectures and their applications. *Neurocomputing* 234, 11–26.
- Makridakis, S., 1989. Why combining works? *Int. J. Forecast.* 5, 601–603.
- Masson, V., 2000. A physically-based scheme for the urban energy budget in atmospheric models. *Bound.-Layer Meteorol.* 94, 357–397.
- Matthews, S.A., Yang, T.-C., 2012. Mapping the results of local statistics: using geographically weighted regression. *Demogr. Res.* 26, 151.
- Mihalakakou, G., Santamouris, M., Asimakopoulos, D., 1998. Modeling ambient air temperature time series using neural networks. *J. Geophys. Res.-Atmos.* 103, 19509–19517.
- Oh, J.W., Ngarambe, J., Duhirwe, P.N., Yun, G.Y., Santamouris, M., 2020. Using deep-learning to forecast the magnitude and characteristics of urban heat island in Seoul Korea. *Sci. Rep.* 10, 3559.
- Oke, T.R., 1981. Canyon geometry and the nocturnal urban heat island: comparison of scale model and field observations. *J. Climatol.* 1, 237–254.
- Oke, T.R., 1982. The energetic basis of the urban heat island. *Q. J. R. Meteorol. Soc.* 108, 1–24.
- Oke, T.R., 2002. Boundary Layer Climates. Routledge.
- Oke, T.R., Spronken-Smith, R., Jäuregui, E., Grimmond, C.S., 1999. The energy balance of Central Mexico City during the dry season. *Atmos. Environ.* 33, 3919–3930.
- Ramezani, H., 2012. A note on the normalized definition of Shannon's diversity index in landscape pattern analysis. *Environ. Natural Res. Res.* 2.
- Ren, Z., Du, Y., He, X., Pu, R., Zheng, H., Hu, H., 2017. Spatiotemporal pattern of urban forest leaf area index in response to rapid urbanization and urban greening. *J. For. Res.* 29, 785–796.
- Ren, Z., Fu, Y., Dong, Y., Zhang, P., He, X., 2022. Rapid urbanization and climate change significantly contribute to worsening urban human thermal comfort: a national 183-city, 26-year study in China. *Urban Clim.* 43.
- Rich, P.M., 1990. Characterizing plant canopies with hemispherical photographs. *Remote Sens. Rev.* 5, 13–29.
- Santamouris, M., Mihalakakou, G., Papanikolaou, N., Asimakopoulos, D.N., 1999. A neural network approach for modeling the Heat Island phenomenon in urban areas during the summer period. *Geophys. Res. Lett.* 26, 337–340.
- Sasaki, Y., Matsuo, K., Yokoyama, M., Sasaki, M., Tanaka, T., Sadohara, S., 2018. Sea breeze effect mapping for mitigating summer urban warming: for making urban environmental climate map of Yokohama and its surrounding area. *Urban Clim.* 24, 529–550.
- Scarano, M., Mancini, F., 2017. Assessing the relationship between sky view factor and land surface temperature to the spatial resolution. *Int. J. Remote Sens.* 38, 6910–6929.
- Scarano, M., Sobrino, J.A., 2015. On the relationship between the sky view factor and the land surface temperature derived by Landsat-8 images in Bari, Italy. *Int. J. Remote Sens.* 36, 4820–4835.
- Schwarz, N., Schlink, U., Franck, U., Großmann, K., 2012. Relationship of land surface and air temperatures and its implications for quantifying urban heat island indicators—an application for the city of Leipzig (Germany). *Ecol. Indic.* 18, 693–704.
- Shaker, R.R., Ehlinger, T.J., 2014. Exploring non-linear relationships between landscape and aquatic ecological condition in southern Wisconsin. *Int. J. Appl. Geosp. Res.* 5, 1–20.
- Smith, S.D., 1988. Coefficients for sea surface wind stress, heat flux, and wind profiles as a function of wind speed and temperature. *J. Geophys. Res.* 93.
- Stewart, I.D., Oke, T.R., 2012. Local climate zones for urban temperature studies. *Bull. Am. Meteorol. Soc.* 93, 1879–1900.
- Sun, Y., Gao, C., Li, J., Wang, R., Liu, J., 2019. Quantifying the effects of urban form on land surface temperature in subtropical high-density urban areas using machine learning. *Remote Sens.* 11.
- Wang, X., Li, Y., 2016. Predicting urban heat island circulation using CFD. *Build. Environ.* 99, 82–97.

- Wang, R., Ren, C., Xu, Y., Lau, K.K.-L., Shi, Y., 2018. Mapping the local climate zones of urban areas by GIS-based and WUDAPT methods: a case study of Hong Kong. *Urban Clim.* 24, 567–576.
- Watson, I., Johnson, G., 1987. Graphical estimation of sky view-factors in urban environments. *J. Climatol.* 7, 193–197.
- Wong, M.M.F., Fung, J.C.H., Ching, J., Yeung, P.P.S., Tse, J.W.P., Ren, C., Wang, R., Cai, M., 2019. Evaluation of uWRF performance and modeling guidance based on WUDAPT and NUDAPT UCP datasets for Hong Kong. *Urban Clim.* 28, 100460.
- Wong, N.H., Tan, C.L., Kolokotsa, D.D., Takebayashi, H., 2021. Greenery as a mitigation and adaptation strategy to urban heat. *Nature Rev. Earth & Environ.* 2, 166–181.
- Wu, S., Wang, Z., Du, Z., Huang, B., Zhang, F., Liu, R., 2020. Geographically and temporally neural network weighted regression for modeling spatiotemporal non-stationary relationships. *Int. J. Geogr. Inf. Sci.* 35, 582–608.
- Xiao, R., Weng, Q., Ouyang, Z., Li, W., Schienke, E.W., Zhang, Z., 2008. Land surface temperature variation and major factors in Beijing, China. *Photogramm. Eng. Remote. Sens.* 74, 451–461.
- Xie, M., Wang, Y., Chang, Q., Fu, M., Ye, M., 2013. Assessment of landscape patterns affecting land surface temperature in different biophysical gradients in Shenzhen, China. *Urban Ecosyst.* 16, 871–886.
- Yang, X., Li, Y., 2015. The impact of building density and building height heterogeneity on average urban albedo and street surface temperature. *Build. Environ.* 90, 146–156.
- Yin, C., Yuan, M., Lu, Y., Huang, Y., Liu, Y., 2018a. Effects of urban form on the urban heat island effect based on spatial regression model. *Sci. Total Environ.* 634, 696–704.
- Yin, C., Yuan, M., Lu, Y., Huang, Y., Liu, Y., 2018b. Effects of urban form on the urban heat island effect based on spatial regression model. *Sci. Total Environ.* 634, 696–704.
- Yuan, F., Bauer, M.E., 2007. Comparison of impervious surface area and normalized difference vegetation index as indicators of surface urban heat island effects in Landsat imagery. *Remote Sens. Environ.* 106, 375–386.
- Yuan, Y., Smith, R.M., Limp, W.F., 1997. Remodeling census population with spatial information from Landsat TM imagery. *Comput. Environ. Urban. Syst.* 21, 245–258.
- Yuan, J., Masuko, S., Shimazaki, Y., Yamanaka, T., Kobayashi, T., 2022. Evaluation of outdoor thermal comfort under different building external-wall-surface with different reflective directional properties using CFD analysis and model experiment. *Build. Environ.* 207.
- Zhang, G.P., 2003. Time series forecasting using a hybrid ARIMA and neural network model. *Neurocomputing* 50, 159–175.
- Zhang, J., Gou, Z., Lu, Y., Lin, P., 2019. The impact of sky view factor on thermal environments in urban parks in a subtropical coastal city of Australia. *Urban For. Urban Green.* 44.
- Zhao, C., Jensen, J., Weng, Q., Weaver, R., 2018. A geographically weighted regression analysis of the underlying factors related to the surface urban Heat Island phenomenon. *Remote Sens.* 10.
- Zheng, Y., Ren, C., Xu, Y., Wang, R., Ho, J., Lau, K., Ng, E., 2018. GIS-based mapping of local climate zone in the high-density city of Hong Kong. *Urban Clim.* 24, 419–448.
- Živković, J., 2020. Urban form and function. *Climate Action* 862–871.